

See discussions, stats, and author profiles for this publication at: <https://www.researchgate.net/publication/216809100>

Direct Observation of the Valence Band Edge by in Situ ECSTM–ECTS in p-Type Cu₂O Layers Prepared by Copper Anodization

ARTICLE in THE JOURNAL OF PHYSICAL CHEMISTRY C · JANUARY 2009

Impact Factor: 4.77 · DOI: 10.1021/jp805915a

CITATIONS

32

READS

159

5 AUTHORS, INCLUDING:



F. Caballero-Briones

Instituto Politécnico Nacional

62 PUBLICATIONS 337 CITATIONS

SEE PROFILE



Juan Manuel Artés

VU University Amsterdam

18 PUBLICATIONS 162 CITATIONS

SEE PROFILE



Ismael Diez-Perez

University of Barcelona

70 PUBLICATIONS 1,554 CITATIONS

SEE PROFILE



Fausto Sanz

University of Barcelona

190 PUBLICATIONS 2,953 CITATIONS

SEE PROFILE

Direct Observation of the Valence Band Edge by in Situ ECSTM-ECTS in p-Type Cu₂O Layers Prepared by Copper Anodization

Felipe Caballero-Briones,^{*,†,‡} Juan M. Artés,^{†,§} Ismael Díez-Pérez,^{†,||} Pau Gorostiza,^{§,⊥,¶} and Fausto Sanz^{*,†,§,⊥}

Laboratory of Bioelectrochemistry and Nanotechnology. Department of Physical Chemistry, Universitat de Barcelona, Martí I Franquès 1, 08028 Barcelona, Spain, Nanoprobes and Nanoswitches Laboratory, Institute for Bioengineering of Catalonia (IBEC), Edifici Hèlix, Baldri i Reixac 15-21, 08028 Barcelona, Spain, CIBER-BBN, Maria de Luna 11, 50018 Zaragoza, Spain, and Institució Catalana de Recerca i Estudis Avançats (ICREA), Passeig Lluís Companys 23, 08010 Barcelona, Spain

Received: July 4, 2008; Revised Manuscript Received: October 27, 2008

Polycrystalline Cu₂O layers have been selectively grown by electrochemical anodization of polycrystalline Cu electrodes in an alkaline medium (pH 12.85). Uniform layers with thicknesses around 100 nm have been obtained. Using electrochemical impedance spectroscopy, it was concluded that the Cu₂O films behave as a p-type semiconductor. The Mott–Schottky plot gives a value for the flat band potential of $U_{\text{FB}} = -255$ mV vs silver/silver chloride electrode (SSC), an estimated carrier density $N_{\text{A}} = 6.1 \times 10^{17} \text{ cm}^{-3}$, and the space charge layer width was calculated to be $W_{\text{SCL}} = 9$ nm at a band bending of 120 mV. The electronic structure of the Cu/Cu₂O/electrolyte interface was for the first time probed by in situ electrochemical tunneling spectroscopy. The use of in situ electrochemical scanning tunneling microscopy allows us to directly observed the valence band edge and determine its position against the absolute energy scale to be $E_{\text{VB}} = -4.9$ eV. Finally, we constructed a quantitative electronic diagram of the Cu/Cu₂O/electrolyte interface, where the positions of the valence and conduction band edges are depicted, as well as the edge of the previously reported electronic subband.

Introduction

Copper(I) oxide (Cu₂O) is an interesting p-type semiconductor material with a direct band gap of 2 eV that has prompted a renewed interest in applications such as resistive random access memories (ReRAM's),¹ anodes in lithium ion batteries,² Cu₂O-covered carbon nanotube catalysts,³ electrochromic devices for solar light modulators⁴ nanocrystalline Cu₂O-based solar cells,^{5,6} and 3D-ordered macroporous materials for photoelectrochemical cells⁷ among others. There is also interest on developing Cu₂O-based transparent conductive oxides (TCO's).⁸

The fabrication of Cu₂O has been usually reported by electrochemical reduction of lactate or citrate Cu(II) complexes onto conductive substrates⁹ or by direct thermal oxidation of Cu¹, but the electrochemical production of technologically useful Cu₂O layers by Cu anodization has been scarcely considered because the anodic copper(I) oxide layers onto polycrystalline Cu have been reported to consist only of a few atomic layers.¹⁰ Nowadays, there are interesting advantages in preparing Cu₂O films by Cu anodization, such as the natural electronic back-contact and the development of a field-induced doping that may improve the electronic behavior of the Cu₂O layers.^{8,10}

The electrochemistry of copper and the oxide development in alkaline media has been extensively studied:^{10–27} the main anodic peaks observed in the potentiodynamic curves are associated first to the formation of Cu₂O ($U_{\text{Cu}_2\text{O}} \sim -400$ mV vs silver/silver chloride electrode; henceforth, SSC), second to the formation of copper(II) oxide (CuO) ($U_{\text{CuO}} \sim +50$ mV vs SSC), and finally to the passivation of the electrode by a duplex layer composed of Cu₂O/CuO–Cu(OH)₂ ($U > 500$ mV vs SSC). In addition to these processes, at potentials negative with respect to Cu₂O formation, the presence of low-current redox peaks has been reported and its importance with respect to the structural evolution of Cu oxides has been also discussed in the literature.^{11–}

From the early works from Droog¹³ and Arvia^{13,14} and that of Burke and Ryan,¹⁵ the processes occurring at potentials previous to the onset of Cu₂O formation have been explained by considering that adsorbed oxygen species in a freshly prepared polycrystalline Cu electrode are formed by a mechanism that involves sequential transitions from lattice Cu atoms (Cu_l) to Cu ad atoms (Cu*) and to Cu ad ions (Cu_s⁺) that eventually lead to Cu⁺-hydrous species, Cu*(OH)_{ad}.¹⁴ The Cu_l can also produce these hydrous species Cu(OH)_{ad}.¹⁴ Copper(I) soluble species, namely, (Cu₂O₂H)[–]_{aq} can also be produced.¹⁴ Cu₂O formation would arise from dehydration of the Cu*(OH)_{ad}/Cu(OH)_{ad} and to a minor extent by heterogeneous nucleation of Cu₂O onto the previously hydroxylated surface.¹⁶

More recently, using in situ electrochemical scanning tunneling microscopy (ECSTM), Matsouka et al.¹⁸ revealed that a commensurate structure appears in a Cu(111) single crystal at $U_{\text{s}} = -950$ mV, disappears at $U_{\text{s}} = -600$ mV, and appears again when the potential is swept back to $U_{\text{s}} = -950$ mV. They

* To whom correspondence should be addressed. Tel.: +34934021240. Fax: +34934021231. E-mail: fsanz@ub.edu (F.S.); fcaballerobriones@ub.edu (F.C.-B.).

[†] Universitat de Barcelona.

[‡] On leave from: CICATA-IPN Unidad Altamira, Km 14.5 Carretera Tampico-Puerto Industrial 89600, Altamira, Tamaulipas, México.

[§] IBEC.

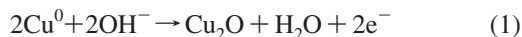
^{||} Current address: Molecular Electronic Research Group, Tao's Laboratory, Department of Electrical Engineering, Goldwater Center Main Campus, Arizona State University, Tempe, AZ 85287-5706.

[⊥] CIBER-BBN.

[¶] ICREA.

suggested that the formed structure corresponds to the surface-bonded copper(I)-hydrous oxide that, in the cathodic sweep, results in the regeneration of active Cu atoms according to the models of Gennero et al.¹⁴ and Burke–Ryan.¹⁵ They also assigned a reversible wave observed at $U_s = -500/-530$ mV to the organization–dissolution process of an ordered oxy–hydroxide adlayer.¹⁸ Maurice et al.,¹⁹ who investigated the initial stages of Cu(111) oxidation in 0.1 M NaOH, observed at about $U_s = -750$ mV a quasi-reversible process assigned to the adsorption–desorption of a 0.19 monolayer of OH[−] together with a simultaneous Cu surface reconstruction.^{10,19} The aforementioned works agree in assigning an important role to this hydroxide sub-monolayer with respect to the further oxide growth as OH adlayer lattice parameters precisely match with those of the oxygen planes in Cu₂O (111).^{10,19,20} The Cu₂O growth starts from the reconstructed OH-populated surface¹⁰ as mentioned before, by a diffusion–dehydration mechanism¹⁴ or/and by heterogeneous nucleation from soluble Cu⁺ species,¹⁶ as the adsorbed OH causes formation of supercritical surface nuclei and depending on the growth potential employed ($U_s = -450$ mV and $U_s = -400$ mV) the thickness, the growth rate, the crystallinity, and the nucleation sites will be affected.¹⁰ At $U_s = -450$ mV, nucleation preferentially takes place in the steps and the oxide layer grows as 2D islands, while, at $U_s = -400$ mV, there are not preferential sites for nucleation and 3D oxide islands are present from the initial stages of the process.

Regarding the Cu₂O growth mechanisms, Kang and Gewirth²¹ suggested that, at pH 13, the Cu₂O growth consumes two hydroxyl ions according to



By using in situ quartz microbalance measurements, Kautek et al.²² observed the net uptake of 2 mol of oxygen atoms to form Cu₂O as in eq 1, suggesting that the Cu₂O differences observed by Kunze et al.¹⁰ at different growth potentials they employed could be associated to the different rates of the two consecutive processes of hydroxyl uptake observed by Kang et al.²¹ An alternative way that can explain the Cu₂O growth is from the solubilized Cu⁺ species that lead to a continuous nucleation–growth mechanism similar to the very well studied chemical-bath deposition process.¹⁶

In the present work, we find that in order to grow sub-micrometer Cu₂O layers it is necessary to achieve completion of the Cu–OH before applying any further oxidation steps, because the OH adlayer acts as the precursor of bulk oxide, forming the necessary nuclei that would form a continuous layer.

Regarding its electronic properties, Cu₂O is well-known for its p-type character.^{4,8,29–35} The p-type behavior has been explained in terms of the presence of stable Cu vacancies (V_{Cu}^+) together with the low probability of hole annihilation.^{4,8,29} Several studies on its electronic structure have demonstrated the existence of electronic states above the top of the valence band (VB) that give rise to a so-called electronic subband (SB).^{20,28} According to Rakhshani,³¹ the SB is in fact composed of two different states: an acceptor state due to Cu vacancies (V_{Cu})^{29,32} located below the Fermi level and with an extension of 0.20 eV, as well as a 0.26 eV donor trap state reported to be composed of oxygen interstitials (O_i).²⁹ The upper limit of the SB is at 0.84 eV above the VB top. Oxygen vacancy (V_{O}) levels with a formation energy higher than that of V_{Cu} should act as “hole killers”²⁹ and are reported to appear at 0.23 and 0.44 eV below the CB minimum³³ (760 mV above the donor level top). Despite the extensive research in the Cu₂O electronic properties principally by spectroscopic techniques, scarce work has been

done for in situ electronic characterization of the Cu/Cu₂O/electrolyte interface.

In situ EC–STM is a powerful tool that can be used either in imaging mode or in spectroscopy mode to obtain direct, local information about the electronic state of the electrode/electrolyte interface without the need of assuming any electronic model.^{36–41} This is particularly useful when dealing with semiconductor/electrolyte interfaces that, commonly studied by impedance methods require assuming an equivalent circuit to extract the complete electronic properties of the studied interface. Cu/Cu oxide/electrolyte interfaces have been consistently studied in the literature^{10,18–20,23,28} although, to the best of our knowledge, measurements in the spectroscopy mode (ECTS) have not been yet reported. Previous studies on ECSTM achieve tunneling only through the SB, mainly because the most commonly used tungsten tips have a limited potential range of electrochemical stability, and thus access to VB states, and more importantly, determination of their energy position within the Cu/Cu₂O/electrolyte interface has been hindered. We have previously reported^{36–42} the Fe/Fe oxide/electrolyte interface studied by ECSTM–ECTS and the results have been plotted as conductance within the whole electrochemical potential range. In that case we were able to directly observe the conduction band (CB) edge,^{36,37} as well as surface states induced by chloride ions in the electrolyte.⁴¹

In the present work, 100 nm thick, polycrystalline, p-type Cu₂O layers have been grown onto polycrystalline Cu substrates in a NaOH electrolyte solution at pH 12.85, using a program of potential steps. The structure and morphology of the emerged films were characterized by X-ray diffraction (XRD) and atomic force microscopy (AFM), and the electronic properties were assessed by electrochemical impedance spectroscopy (EIS), ECSTM, and ECTS, the latter being successfully applied for the first time on the Cu/Cu₂O/electrolyte interface. The final picture of the quantitative electronic diagram in an absolute energy scale locating the edges of VC and SB is proposed.

Experimental Section

Sample and Electrolyte. Cu₂O layers were prepared onto polycrystalline Cu disks (99.99% from Goodfellow) of 10 mm diameter \times 1 mm thickness that were sequentially polished with Al₂O₃ emery paper of 9, 3, and 1 μm and finally with Al₂O₃ paste up to 0.3 μm . After polishing, the disks were ultrasonically rinsed with Milli-Q (MQ) water and isopropyl alcohol and afterward Ar-blown. Electrode surfaces were mirrorlike and presented a root mean square (rms) roughness on the order of 5 nm (taken from 5 μm \times 5 μm AFM images). The electrolyte employed in the electrochemical cell was 0.15 M NaOH prepared from pro analysis purity grade chemicals from Riedel de H  en and MQ water (typically 18 M  ). The electrolyte was always freshly prepared, and its measured pH ranged from 12.8 to 13.0. Before each experiment the electrolyte was bubbled with Ar (99.999%) by 60 min to remove dissolved O₂/CO₂.

Electrochemical Measurements. The anodization of the Cu electrodes, the voltammetric curves, and the impedance measurements were performed using a PGSTAT 12 Autolab potentiostat (Ecochemie) equipped with a frequency analyzer module (FRA). A standard glass cell was used with the working electrode placed at the bottom, with a large surface Pt/Ir wire as auxiliary electrode and a SSC reference electrode in electric contact with the solution through a Luggin capillary. All the potentials from herein will be quoted versus this electrode. The EIS were done at an excitation signal of 25 mV amplitude (in the order of kT energy). The impedance vs frequency spectra

were acquired at fixed sample potentials. Afterward, impedance vs potential measurement at different frequencies was performed and the data are represented as Mott–Schottky plots ($1/C^2$ vs U_s) to extract the information of flat band potential (FB), semiconductor type, and carrier density (N).

Film Growth. Prior to film growth, a cyclic voltammogram (CV) was acquired to verify the position of the OH adsorption and copper(I) oxide formation peaks. Cu_2O films were then grown following a version of a previously employed stepwise routine for other oxides:³⁷

(1) The native oxide was reduced by applying a high negative potential. Then, to ensure a metallic Cu surface and to avoid sudden current spikes, the sample potential was stepped in 100 mV increments, leaving the sample at each step by 5 min, up to $U_s = -1000$ mV.

(2) Once the current was stabilized, the potential was stepped to the OH-adsorption potential range and left 5 min to allow the formation of the hydroxide.

(3) The potential was then stepped to the onset potential of Cu(0) to Cu(I) oxidation ($U_s = -430$ mV) and left until the transient current stabilizes.

(4) The potential was stepped to a potential of surface passivity (corresponding to the presence of a current plateau ($U_s = -330$ mV) before the onset of the Cu(I) to Cu(II) oxidation).

(5) The electrode was finally either removed in vivo, rinsed with MQ water, Ar-blown, and stored in the dark to be characterized ex situ or, alternatively, left at $U_s = -330$ mV to perform in situ electrochemical measurements.

The obtained Cu_2O layers have uniform and smooth surfaces, and they are remarkably stable upon aging. The optical band gap (E_g) was calculated to be 2.0 eV, as determined from reflectance measurements of the $\text{Cu}_2\text{O}/\text{Cu}$ heterostructure.

Structural Measurements. The $\text{Cu}_2\text{O}/\text{Cu}$ layers were measured by XRD using unfiltered Cu K α radiation, in a Siemens D500 diffractometer in the grazing incidence geometry. Different incidence angles (0.4, 0.8, and 1.2°) were used to look for the best intensity/noise ratio. The phases were identified within the PDF database.⁴³

Scanning Probe Measurements. The morphology of the electrode surface after anodization was studied by ex situ AFM using a Multimode microscope head controlled with a Nanoscope IIIa electronics (Veeco Metrology Group, Santa Barbara, CA). All the images were performed in air, in the intermittent contact mode with Si cantilevers of 35 N/m spring constants (Nanosensors, Wetzlar-Blankenfeld, Germany).

The ECSTM and ECTS studies were performed at room temperature by using a Molecular Imaging microscope head (Agilent, Phoenix, AZ) controlled by the Nanoscope IIIa electronics. The STM electrochemical cell was made of Teflon and exposes a 0.30 cm² area to the solution delimited by an O-ring. A Pt/Ir wire concentric to the sample was used as auxiliary electrode, and a SSC electrode was used as true reference. ECSTM tips were prepared with the procedure described elsewhere.³⁸ The faradaic tip current at potentiostatic conditions and far from the surface was typically better than 0.1 nA for imaging studies, and better than 0.01 nA for spectroscopic recordings. The STM images were recorded in the constant current mode at typical current setpoints ranging from 0.50 to 2.0 nA. A CV was acquired before each set of experiments to verify the state of the oxide and the range of sample potentials. Images were acquired at different sample potentials and using the entire electrochemical range of the tip while recording imaging conditions. Before image acquisition,

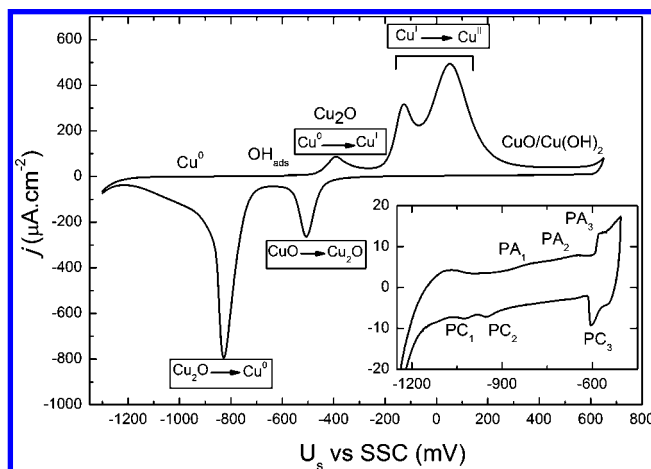


Figure 1. CV of a Cu electrode in 0.15 M NaOH. Potential sweep rate of 10 mV s⁻¹. Inset: detail of the potential range negative with respect the onset of Cu⁰ to Cu(I) oxidation.

the sample current was allowed to stabilize for 5 min. The AFM and ECSTM images were analyzed with the WSxM freeware v.4.0 Develop 8.21.⁴⁴

The ECTS setup and methodology is extensively described elsewhere.^{36–42} Briefly, the measurements were performed with a freshly prepared STM tip engaged at a current setpoint of 1.5 nA. Feedback was momentarily disconnected, and a potential ramp was applied to the tip. The tunnel current was recorded and digitized in real time with a digital oscilloscope (Tektronix). Blank curves with the tip placed far from the surface were also recorded to subtract the contribution of the nontunneling “leakage” current. Spectra were acquired at different sample potentials within the range of electrochemical stability of the oxide. Conductance vs sample potential curves were obtained by differentiating the ECTS spectra after smoothing to minimize noise due to the differentiation algorithm.³⁹ The electrochemical potentials were converted to the electron scale vs the vacuum level, using the relationship E_{vac} (eV) = $-e(U_s + 4.35)$,^{34,45} where 4.35 eV is the work function of Cu measured by UPS.³⁴

Results and Discussion

Cyclic Voltammetry. Figure 1 shows a CV obtained from a Cu electrode in contact with a 0.15 M NaOH electrolyte solution, at a sweep potential rate of 10 mV/s. The CV was obtained by first sweeping from negative to positive potentials. In the anodic sweep, the first electroodic peak appearing in the range of potentials between $U_s = -550$ mV and $U_s = -250$ mV has been associated with the Cu(0) to Cu(I) oxidation and the subsequent formation of Cu_2O .^{20,21,24} The two peaks observed in the potential range lying from $U_s = -250$ mV to $U_s = +500$ mV correspond to the further oxidation of Cu(I) to Cu(II), followed by the formation of the passive layer. Some authors report this final film to be a duplex layer of Cu_2O and $\text{CuO}-\text{Cu}(\text{OH})_2$.^{20,21,24} The cathodic peaks observed from $U_s = -500$ mV to $U_s = -800$ mV are respectively attributed to the Cu(II) to Cu(I) reduction and Cu(I) to Cu(0).^{20,21,24} At negative potentials prior to the first anodic peak, we used the label OH_{ads} in the CV to indicate a series of processes involving OH^- adsorption.^{10,18,19} As the aim of the present work is the formation and properties of Cu_2O films, only the potential range from $U_s = -1200$ mV to $U_s = -200$ mV, from hydrogen evolution reaction (HER) to Cu_2O formation will be analyzed.

The inset in Figure 1 shows a CV made in the potential range labeled OH_{ads} that corresponds to the processes attributed to

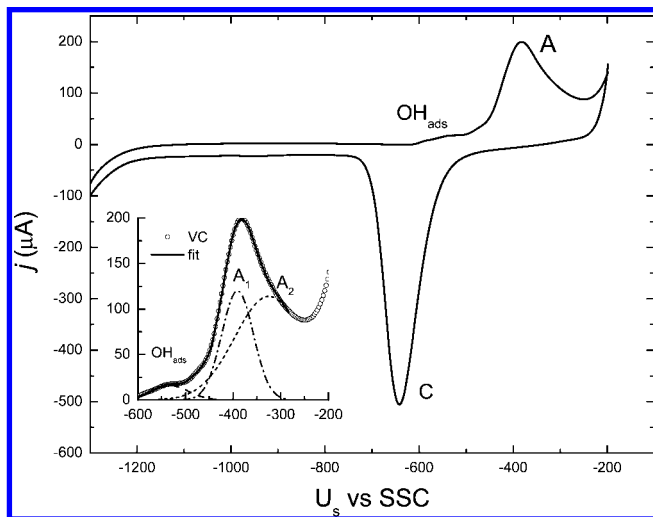


Figure 2. Cyclic voltammogram in the potential region below the Cu₂O peak in 0.15 M NaOH. Potential sweep rate of 10 mV/s. Inset: detail of the A peak with Gaussian fit.

hydroxyl adsorption. In the CV from $U_s = -1250$ mV to $U_s = -450$ mV, three anodic peaks at $U_s = -800$ mV, $U_s = -650$ mV, and $U_s = -575$ mV and the corresponding cathodic peaks at $U_s = -605$ mV, $U_s = -950$ mV, and $U_s = -1025$ mV respectively labeled PA₁, PA₂, PA₃, PC₃, PC₂, and PC₁ can be observed. The anodic and cathodic peaks of the PA₁–PC₁ and PA₂–PC₂ pairs are separated by about 300 mV, while the peaks of the redox couple PA₃–PC₃ are observed at the same potential, a characteristic associated with an adsorption process. Reprising the aforementioned results of Matsuoka¹⁸ and Maurice¹⁹ and the model proposed by Burke,¹⁵ the assignment of the redox pairs PA₁–PC₁ and PA₂–PC₂ respectively to an adion formation and to the subsequent hydrous oxide development seems to be straightforward. The reversible PA₃–PC₃ redox pair can be ascribed to the proper adsorption–desorption process of hydroxyl ions.^{18,19} The calculated charge transferred in this potential region, yields $63 \mu\text{C} \cdot \text{cm}^{-2}$ in fine agreement with the ca. 0.2 monolayer adsorption of hydroxyl ions as pointed out in the literature.^{10,19,20}

In Figure 2, the potential scan is extended to show the anodic peak A associated with Cu(0) to Cu(I) oxidation and Cu₂O formation. The maximum of the anodic peak is centered on $U_s = -375$ mV, and its asymmetric shape suggests a nonelementary electron-transfer reaction. The corresponding cathodic peak C related with Cu(I) to Cu(0) reduction is centered at $U_s = -650$ mV. The peak potential shift has been reported to be characteristic of a constant high-field growth mechanism by ion transport through the oxide.^{10,22} By quartz microbalance measurements²² it has been determined that the reduction of the oxide is only complete when the potential is swept back to around $U_s = -1100$ mV. Finally at more positive potentials with respect to peak A a current plateau (about $U_s = -260$ mV) followed by the onset potential of the peak related with Cu(II) formation at about $U_s = -200$ mV are also observed.

The asymmetry observed in the A peak indeed reflects the consumption of two hydroxyl ions in a step mechanism where the rate-limiting step would be an OH[−] diffusion–dehydration process, accordingly with the suggestion of Kang²¹ and Kautek.²² With this assumption peak A may be deconvoluted into Gaussian separated peaks. In the inset of Figure 2, an example of such a deconvolution procedure after baseline subtraction is presented: between $U_s = -600$ mV and $U_s = -500$ mV the OH-adsorption processes were fitted by the peak labeled OH_{ads}.

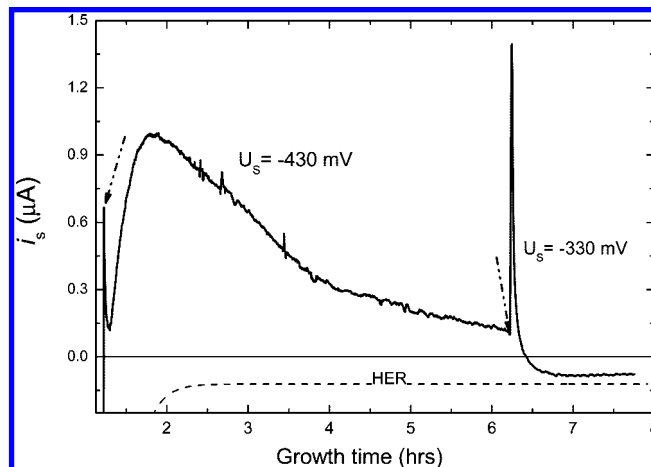


Figure 3. Current transients of the growth process at $U_s = -430$ mV and $U_s = -330$ mV. $U_s = -430$ mV, and $U_s = -330$ mV potential application instants are marked by arrows.

The main peak is fitted to two Gaussian peaks: (a) a sharp peak labeled A₁, which could be associated with the reaction of the previously adsorbed surface hydroxyl to give rise to a CuOH-like phase, and (b) a wider peak labeled A₂, which would correspond to the diffusion of hydroxyl ions to the electrode surface, and the eventual dehydration of the copper hydroxide to lead the Cu₂O phase.²¹ It is noteworthy that the peaks overlap, suggesting that both processes take place simultaneously in this potential range. A more detailed study of the behavior of the anodic peak A at different sweep rates and electrolyte concentration is actually on run.

Cu₂O/Cu Growth. As mentioned in the Experimental Section, after reduction of the native oxide, to obtain the OH adlayer needed as a precursor surface to promote the oxide growth, the potential was stepped to the OH-adsorption potential region. No further current change was observed after keeping the potential for 5 min. Figure 3 presents the chronoamperometric response (CA) obtained during the oxide growth after stepping the potential to $U_s = -430$ mV, corresponding to the maximum increase rate of the anodic peak A₁, and the subsequent evolution with time after applying a second step up to $U_s = -330$ mV, that correspond with the maximum of the A₂ peak. The dashed curve represents the exponential fit of the HER current that accounts for the reference current limit. In the figure a short transient can be noticed upon application of a potential step from the OH_{ads} range to $U_s = -430$ mV; the curve exhibits a nucleation spike, followed by a steep current increase that reaches a maximum at about 2 h and then decreases. Stepping the potential up to $U_s = -330$ mV caused a sharp current transient that ends in the current reference level, characteristic of a passivated surface. The behavior of the CA curve agrees with the proposed mechanism that involves a surface process associated with creation of nuclei followed by a diffusion-controlled process that accounts for the growth of the grains, ascribed to proposed anodic peaks A₁ and A₂. From the transferred charge, the thickness of the layer was estimated to be about 100 nm, in the order of current technological applications.¹

Morphology of the Cu₂O Layers. Parts A and B of Figure 4 show AFM topographic images of the Cu₂O layer morphology. The roughness was calculated to be $R_{\text{rms}} = 17.2$ nm compared with $R_{\text{rms}} = 7.2$ nm for the Cu substrate, and the average grain size was estimated to be 90 ± 2 nm. In Figure 4C three profiles taken through different scan lines are presented, and it can be appreciated that grains from 50 to 100 nm are present and they

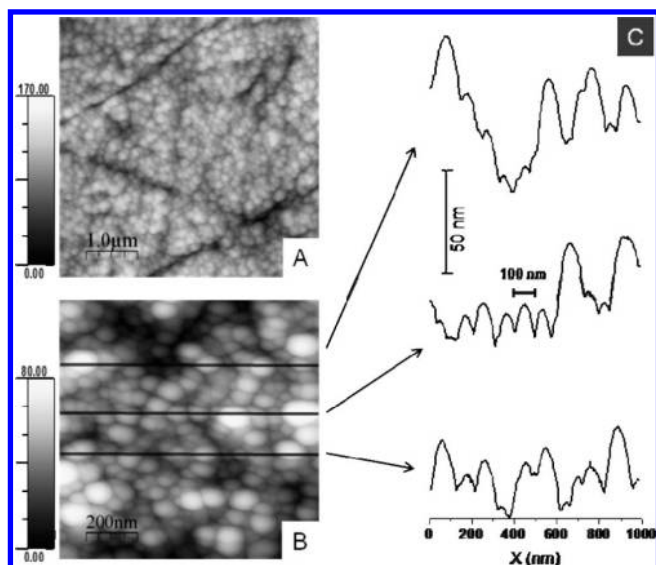


Figure 4. (A) $5 \times 5 \mu\text{m}^2$ and (B) $1 \times 1 \mu\text{m}^2$ AFM images obtained over the emerged Cu_2O layer. (C) Profiles obtained in the B image through the indicated scan lines.

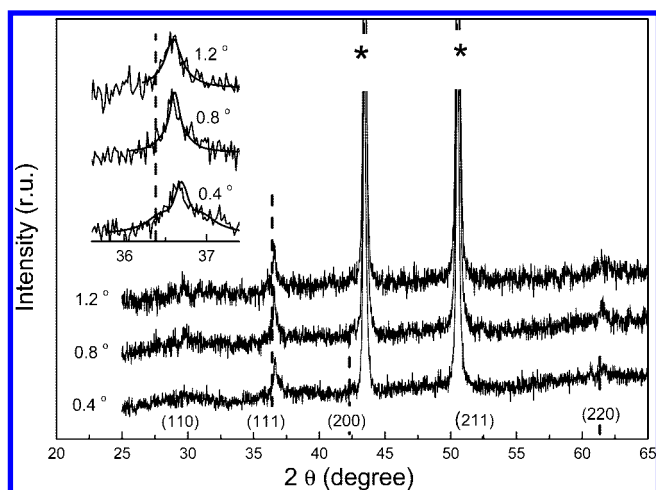


Figure 5. Grazing incidence X-ray diffractograms of a $\text{Cu}_2\text{O}/\text{Cu}$ heterostructure at three incidence angles. Inset: detail of the main cuprite peak.

grow one over each other. The increase in roughness together with the wide size distribution of the grains indicates that the growth mechanism includes continuous nucleation and growth processes,¹⁶ in agreement with the voltammetric results. During polarization at -430 mV the copper migrates through the oxide layer as mentioned before, reaching the surface and then providing ions that together with OH^- diffusing from the solution account for crystal growth.

Layer Structure. Figure 5 presents the X-ray diffractograms of the $\text{Cu}_2\text{O}/\text{Cu}$ heterostructure measured at three incidence angles. Peaks related with the (110), (111), (200), and (220) cuprite planes are observed, the main cuprite peak being the (111) reflection.⁴³ The reflections corresponding to the Cu electrode are marked with an asterisk. The intensity of the main cuprite reflection is similar at the three incident angles, and the intensities of the (110) and (220) planes seem to increase with the incidence angle, according to a suggested mechanism of strain release during the film growth.¹⁰ The inset of the figure features the detail of the main diffraction peak of the Cu_2O layer fitted to pseudo Voigt functions. The (111) peak position displaces to higher Bragg angles as the incidence angle decreases and the estimated lattice parameter at a beam incidence of 1.2°

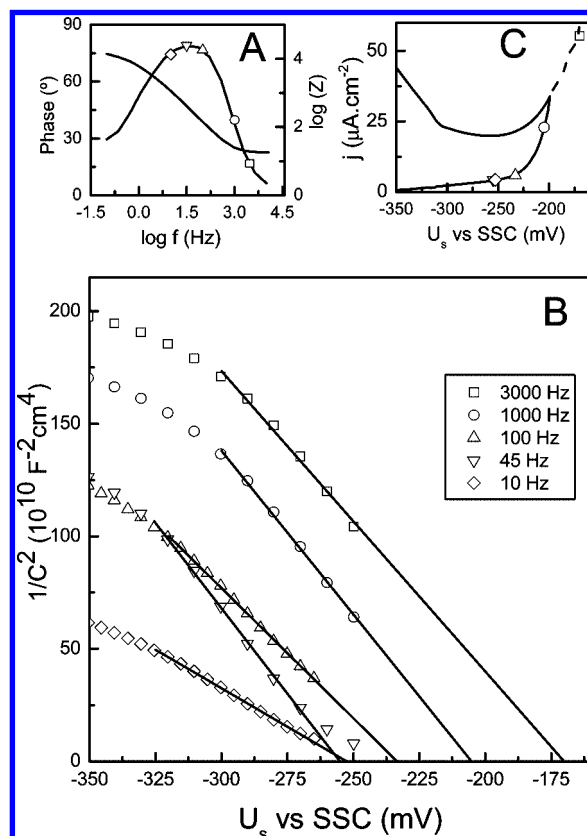


Figure 6. (A) Bode representation of the impedance of the Cu_2O layers at $U_s = -375$ mV. (B) Mott–Schottky plots at different excitation frequencies (f), within the $1/C^2 = 0$ extrapolation corresponding to the $U_{\text{FB}}(f)$. (C) CV in 0.15 M NaOH, pH 12.85 in the MS region, featuring the $U_{\text{FB}}(f)$. Symbols in each graph correspond to the same f .

gives a value of $a_{(111)} = 4.53$ Å, above to the bulk cuprite value $a = 4.27$ Å, probably due to the effect of a stress gradient through the film thickness, caused by the restructuring of the Cu–OH surface to accommodate the lattice of Cu_2O .²⁶ The corresponding crystallite size was estimated from the Debye–Scherrer formula to be $d_{(111)} = 36$ nm. The other Cu_2O reflections are too weak to allow a reliable calculation.

Capacitance Measurements. Parts A–C of Figure 6 summarize the results of the capacitance measurements on the Cu_2O film. Figure 6A shows the Bode plot of the Cu_2O film, which comprises the phase and the impedance (Z) values versus the logarithm of the applied frequency ($\log f$). The phase presents its maximum value at $f = 45$ Hz which is associated with a process with almost pure capacitive behavior. To perform the capacitance–potential measurements, we chose $f = 45$ Hz as well as $f = 10$ Hz and $f = 100$ Hz, at both sides of the phase maximum, and $f = 1$ kHz and $f = 3$ kHz for comparison with other works.^{37,46,47} The symbols in the Bode plot (Figure 6A) denote the frequencies where these measurements were performed. The capacitance was obtained assuming an RC (resistance-capacitor) equivalent circuit, and the data were represented as a Mott–Schottky (MS) plot following

$$\frac{1}{C^2} = \frac{1}{N_A e \epsilon_0 \epsilon} \left[(U_s - U_{\text{FB}}) - \frac{kT}{e} \right] \quad (2)$$

where C is the space charge capacitance in the semiconductor; N_A the hole carrier density; e the elemental charge value; ϵ_0 the permittivity of the vacuum; ϵ the relative permittivity of the semiconductor, assumed here to be 7.6 for Cu_2O ;⁴⁸ and k the Boltzmann constant.

TABLE 1: Flat Band Potential and Carrier Density Calculated from the Mott–Schottky Plots at Different Frequencies

frequency (Hz)	flat band potential (mV)	carrier density (cm ⁻³)
100	−233	8.00×10^{17}
45	−255	6.12×10^{17}
10	−253	1.36×10^{18}

The MS plots are represented in Figure 6B as $1/C^2$ vs U_{sample} , and to estimate the flat band potential (U_{FB}), the linear part of the data was extrapolated to $1/C^2 = 0$.^{37,46} The negative sign of the slope in the MS plot indicates the p-type character of the layer, and N_A was calculated from the value of the slope.^{37,46} In Figure 6B,C, it can be observed that the $1/C^2$ extrapolation depends on the chosen working frequency, shifting toward higher U_{FB} values, but the U_{FB} values obtained at $f = 1$ kHz and $f = 3$ kHz lie within the onset potential for Cu₂O oxidation to copper(II) oxide.²⁰ Due to the uncertainty of the values obtained at these frequencies, in Table 1, only the N_A and the U_{FB} values obtained at $f = 10$ Hz, $f = 45$ Hz, and $f = 100$ Hz are presented.

The obtained U_{FB} values are in agreement with the values obtained by Nakaoka by the same technique²⁷ on a Cu₂O layer prepared by electroreduction of a CuO/Pt film and with those of Strehblow et al. obtained by photocurrent spectroscopy.²⁰ The calculated carrier density for the Cu₂O films, about 10^{18} cm⁻³, is between the reported values for electrodeposited Cu₂O films (10^{15} – 10^{16} cm⁻³),^{31,50} and the values reported by Nakaoka (10^{20} cm⁻³),²⁷ suggesting that our preparation technique induces an increase in the density of vacancies with respect to electrodeposition method. The variation of the carrier density with the frequency suggests that a mixed electronic–ionic conduction mechanism could be implicated in the Cu₂O/Cu device as suggested by Rosenstock et al.³⁵ The high mobility of V_{Cu} in the solid supports this assumption.⁴⁸ The confirmation of this mixed electronic–ionic conduction mechanism for the passive Cu₂O layers will be the subject of a future work.

Additionally, it is possible to estimate the width of the space charge layer (W_{SCL}) of the semiconductor as it is related with the capacitance through $(1/2)(W_{\text{SCL}}) = (\epsilon_0/C)^{1/2}$.^{46,47} The corresponding calculation yields $W_{\text{SC}} = 9$ nm for the Cu₂O/Cu layer, a higher value than the one we obtained for the iron oxide passive layer ($N_D \sim 10^{21}$ cm⁻³),³⁷ as correspond with a lower doping level in Cu₂O.⁴⁶ The determinations of U_{FB} , N_A , and W_{SCL} are required to depict the energy diagram of the Cu/Cu₂O/electrolyte interface, and complementary data such as the energy location of the main electronic scales at our interface are achieved using ECSTM and ECTS.

Study of the Electronic Properties of the Cu₂O/Cu by ECSTM and ECTS. We used ECSTM–ECTS to probe the main energy levels at electrode potentials around U_{FB} . Figure 7 shows a set of ECSTM images obtained at a constant applied electrode potential $U_s = -230$ mV, which corresponds to a slight hole accumulation at the oxide surface. We varied the potential of the probe from $U_{\text{tip}} = +775$ mV to $U_{\text{tip}} = -500$ mV. In the same figure, an adapted scheme of the band structure of the Cu₂O film following the previous model of Strehblow et al.²⁰ is presented, where, additionally to the main semiconductor bands (valence band (VB) and conduction band (CB)), a semifilled subband (SB) above the VB is also represented. The vacuum energy scale was set as $E(\text{eV}) = -e(U_s + 4.35)$.^{34,45} U_s was placed at -230 mV such that the Fermi level was set in the middle of the SB.²⁰ The limits of the bands were intentionally left vague for the more detailed band structure analysis we will present at the ECTS section.

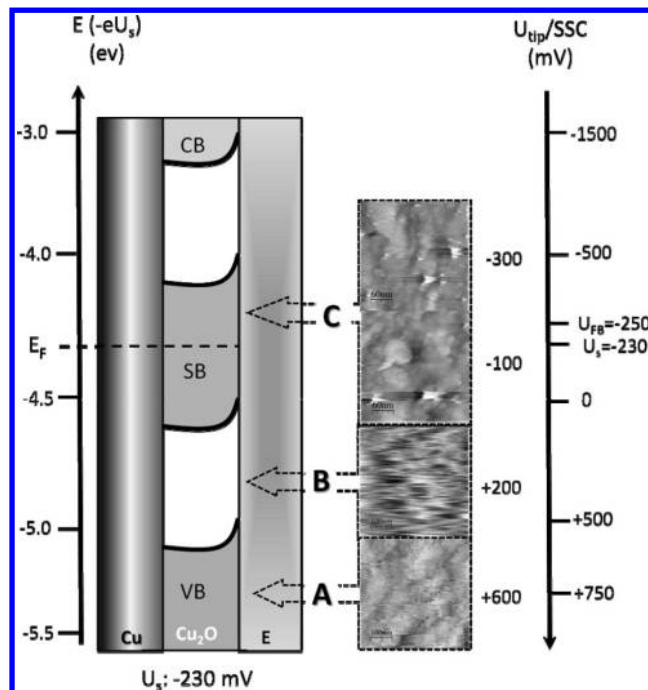


Figure 7. Scheme of the band structure of the Cu/Cu₂O/electrolyte interface.²⁰ The ECSTM images were obtained in the same surface area of the Cu₂O film maintained at a fixed $U_s = -230$ mV in pH 12.85 NaOH solution. Images were acquired at the U_{tip} indicated rightwards. Scan size: 500×500 nm², $I_{\text{setpoint}} 1.5$ nA. Z scale is 100 nm.

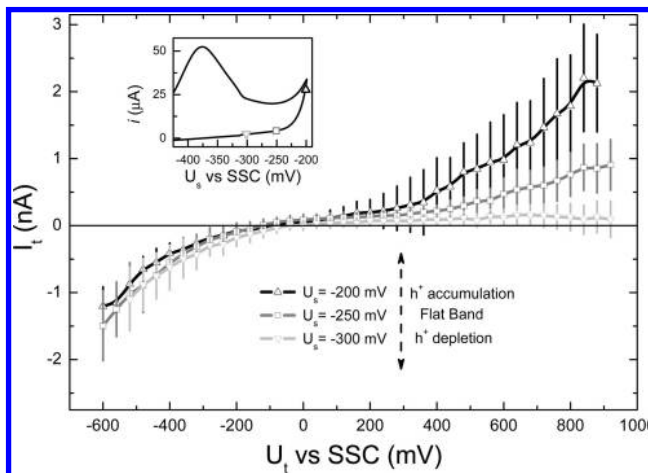


Figure 8. ECTS spectra obtained in the Cu/Cu₂O/electrolyte interface at different U_s . Inset: CV with the indicated position of each U_s .

In Figure 7, three tunnel ranges are indicated: A–C, according to the U_{tip} range. In range A, $U_{\text{tip}} > +550$ mV, good tunneling conditions and stable, reproducible images are obtained. The same was observed in the current vs time traces for the tunneling setpoint current. In range B, $+550 < U_{\text{tip}} < 0$ mV, transient images were obtained: after a couple of scans the image gets unstable or even disappears; the vanishing images were obtained when varying U_t from more positive to less, but when U_t was varied in the reverse way, no image is obtained upon U_t being very close to $+550$ mV. Finally, in range C, $0 < U_{\text{tip}} < -500$ mV, stable images and tunnel current were again recovered. At tip potentials above $U_{\text{tip}} = +775$ mV and below $U_{\text{tip}} = -500$ mV the surface is being clearly modified upon continuing tip scan, as evidenced by sudden bright spots. According to the reported position of the Cu₂O VB of with respect to the Cu Fermi level²⁰ and the work function of Cu³⁴ that allow the direct

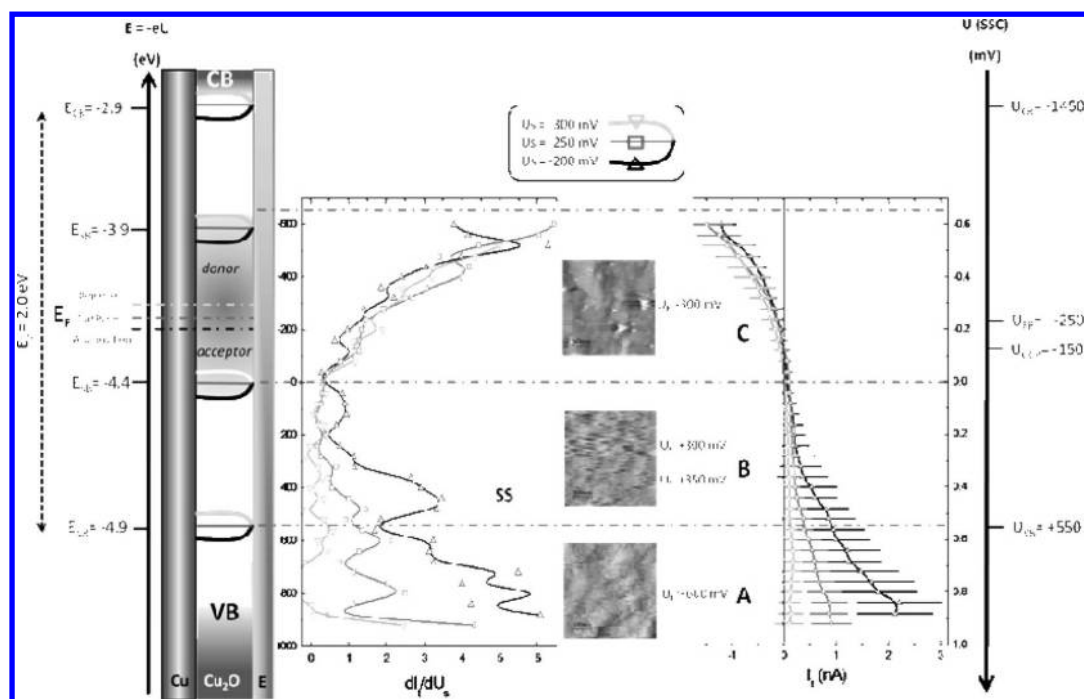


Figure 9. Right panel: ECTS spectra obtained at different electrode potentials ($U_s = -200$ mV; $U_s = -250$ mV; $U_s = -300$ mV). U_{tip} scanning with a 15 V/s ramp. In the right scale are indicated the measured U_{FB} and U_{OCP} of the Cu/Cu₂O/electrolyte interface. The ECSTM images 500×500 nm² were acquired at $U_s = -230$ mV at $I_{setpoint} = 1.5$ nA and different U_{tip} (shown at right side of each image), vertical scale in images is 100 nm. Central panel: Conductance dI_{tip}/dU_s obtained from the ECTS spectra. Left panel: Electronic band diagram for the Cu/Cu₂O/electrolyte interface. Right scale takes $E_{vacuum} = 0$.

conversion between electrochemical potential and electronic energy, we can conclude that the images obtained in range A correspond to tunneling through the VB which, to the best of our knowledge, has never been reported. Correspondingly, the images obtained in the C range should be ascribed to the tunneling through the SB.²⁰ The evanescent images obtained in the B range and the hysteresis observed when changing the U_t scanning direction could arise by the presence of surface states, although further work is needed to support this explanation.

ECTS Characterization of Cu₂O. Electrochemical tunneling spectra, tip current vs tip potential (I_t vs U_t), were acquired using the previously reported setup.^{36–42} Figure 8 presents three ECTS spectra corresponding to three fixed sample potentials ($U_s = -300$, $U_s = -250$ and $U_s = -200$ mV) whose positions in the voltammogram are shown in the inset. These sample potentials are within the range of Cu₂O electrochemical stability, where neither oxidation nor reduction occurs, and are characterized respectively by slight depletion, near FB potential, and slight accumulation of holes. Each solid curve in Figure 8 is the average of 15 experimental curves and the error bars correspond to their standard deviation.^{37,40}

ECTS spectra correspond to the expected behavior of a p-type semiconductor when the U_s varies from positive to negative overpotentials with respect to the U_{FB} : when the electrode is in accumulation of holes ($U_s = -200$ mV), a high tunneling current in the anodic branch of the spectra is observed. As the surface space is depleted of charge carriers upon U_s reduction ($U_s = -300$ mV), the tunneling current in the anodic branch progressively reduces, while the cathodic branch is almost unchanged. It is very interesting to note that the current behavior is the opposite to that observed in *n*-iron(III) oxide,⁴⁰ where the dependence of the tunneling current was related with the population of the corresponding majority carriers involved (electrons, in that case). In *n*-iron(III) oxide, we observed that the tunneling current increases at overpotentials more negative

than its U_{FB} , correspondingly with an accumulation of electrons. Our new results demonstrate the feasibility of the ECTS technique to explore the electronic properties of any semiconductor under electrochemical conditions, as we present for the first time the in situ electronic characterization of the Cu/Cu₂O/electrolyte interface.

Figure 9 abridges this electronic characterization of the interface, representing the ECTS tip current vs tip potential (I_t vs U_t) spectra, the interface conductance (dI_{tunnel}/dU_s) spectra against the same tip potential, and the ECSTM images obtained at $U_s = -230$ mV and separated in the three ranges A–C, together compared with the new band diagram constructed amid the previously discussed results.⁴¹ Building up the band diagram, the following data were used: the FB potential, $U_{FB} = -250$ mV, obtained from EIS; the Cu/Cu₂O/electrolyte open circuit potential, $U_{OCP} = -150$ mV, measured after the layer was grown; the gap energy, $E_g = 2.0$ eV, we obtained from reflectance measurements. Other data were as follows: the VB edge $U_{VB} = +550$ mV, calculated from ref 20, and the energy of the CB edge, $U_{CB} = -1450$ mV, calculated using the values of the VB_{top} and the gap energy. The bottom of the SB was set at $U_s = 0$ mV and the top at $U_s = -500$ mV considering the B potential range in Figure 7, which gives a difference between VB_{top} and SB_{bottom} of 550 mV, in the range of previously reported values,^{8,29,31,32} and a difference from SB_{top} to CB_{bottom} of 900 mV. The “donor” and “acceptor” labels in the SB correspond to reported localized states.^{8,25,27,28} The band bending is shown for each $E_F = -e(U_s + 4.35)$, as well as the positions of the VB and CB edges in the absolute energy scale.

Figure 9 will be discussed by reprising the procedure developed to analyze Figure 7, by the definition of the three potential ranges yet depicted, A–C:

The A range ($U_t > +550$ mV) is characterized by good imaging conditions. The tip current values are positive, consistently with holes transfer from the tip to the VB. The

conductance increases as holes accumulate at the surface space ($U_s = -200$ mV) and decreases sensitively when holes are removed at $U_s = -300$ mV. The outstanding result is that by the first time, direct electronic probe of the VB was achieved under electrochemical conditions.

The B range ($+550 < U_t < 0$ mV) is where only evanescent images depending on the U_t scanning direction were obtained. The tunneling current in this range passes through zero, but in the conductance spectra (central plot) an interesting feature is highlighted when the sample potential is fixed at $U_s = -200$ mV: when scanning the tip through $U_t = -450$ mV a maximum peak value in the dI/dU_s plot suggests that the accumulation of holes would induce transient surface states (marked as SS in Figure 9), as suggested before. These SS were overcome in the Mott–Schottky measurements, because in that case spectra were obtained in deep depletion conditions ($U_s = -375$ mV).

The C range ($0 < U_t < -500$), also named SB range, is where imaging by ECSTM is again possible, yet reported in literature.^{10,18–20,23,28} The cathodic branch of the ECTS spectra is almost constant, indicating that the population of carriers in the SB is practically unaffected by the applied potential, confirming this SB should consist of trap-states as suggested by Rakshani.⁴¹ Indeed, the SB has been mentioned to be composed by V_{Cu} states that at a first glance should remain unaffected in the U_s potential range of Cu₂O stability, until further oxidation to Cu(II) occurs at more positive U_s . The conductance plot also appears almost unaffected by the U_s ; no distinction between acceptor and donor states can be done. Interestingly, ECTS spectra at $U_s = -200$ mV are quite symmetrical, suggesting that the relative conductance of the VB and SB at this potential is very similar. Further characterization should make it possible to estimate the density of states in the SB and compare to reported values by other techniques.

Summarizing, we were able to directly measure the VB edge, and the energy position of the bands with respect to the VB_{top} is very consistent with the values reported by other authors,^{20,30,32} confirming the effectiveness of the ECTS technique to directly probe electronic states on oxide/electrolyte interfaces.

Conclusions

We were able to prepare sub-micrometer thick, polycrystalline Cu₂O/Cu layers by an electrochemical routine with potentiostatic control. The layers crystallize in the Cu₂O cuprite form, achieving a thickness up to 100 nm, and they behave as p-type semiconductors. By impedance measurements the flat band potential was determined at 45 Hz to be $U_{FB} = -255$ mV, the density of carriers was estimated to be $N_A = 6.12 \times 10^{17}$ cm⁻³ and the width of the space charge layer was determined to be $W_{SC} = 9$ nm. The electronic properties of the layers were further studied by EC-STM imaging and ECTS, reporting the first tunneling spectroscopy characterization of the Cu₂O/electrolyte interface. The valence band edge and subband edge above the VB were directly observed by EC-STM imaging and ECTS, and a quantitative electronic band diagram was proposed to summarize the whole data of the electrochemical system.

Acknowledgment. F.C.-B. thanks Instituto Politécnico Nacional (México) the financial support through a COTEPABE license. P.G. acknowledges financial support from the Ministerio de Educación y Ciencia through the Ramón y Cajal program and PETRI Project PET2006-0808. We recognize the technical support from Ms. A. Palacios and Mr. Ivan Rimmaudo and from the Scientific-Technical Services of the University of Barcelona,

especially Dr. J. Bassas (XRD unit) and Dr. J. Díaz and Dr. G. Oncins (Nanometric Techniques unit). This work was partially financed with the CTQ2007-68101-C02-01 project from the Ministerio de Educación y Ciencia, Spain.

Supporting Information Available: Text and figures showing the effect of preferential orientation of the Cu substrate surface, the effect of Cu²⁺ dissolution, and topographic features in ECSTM images. This material is available free of charge via the Internet at <http://pubs.acs.org>.

References and Notes

- (1) Dong, R.; Lee, D. S.; Xiang, W. F.; Oh, S. J.; Seong, D. J.; Heo, S. H.; Choi, H. J.; Kwon, M. J.; Seo, S. N.; Pyun, M. B.; Hasan, M.; Hwang, H. *Appl. Phys. Lett.* **2007**, *90*, 042107.
- (2) Fu, L. J.; Gao, J.; Zhang, T.; Cao, Q.; Yang, L. C.; Wu, Y. P.; Holze, R. *J. Power Sources* **2007**, *171*, 904.
- (3) Yu, Y.; Ma, L.-L.; Huang, W.-Y.; Li, J.-L.; Wong, P.-K.; Yu, J. C. *J. Solid State Chem.* **2005**, *178*, 1488.
- (4) Ristova, M.; Neskovska, R.; Mirčeski, V. *Sol. Energy Mater. Sol. Cells* **2007**, *91*, 1361.
- (5) Lee, Y.-H.; Leub, I.-C.; Wu, M.-T.; Yen, J.-H.; Fung, K.-Z. *J. Alloy Compds.* **2007**, *427*, 213.
- (6) Rai, B. P. *Sol. Cells* **1988**, *25*, 265.
- (7) Li, X.; Tao, F.; Jiang, Y.; Xu, Z. *J. Colloid Interface Sci.* **2007**, *308*, 460.
- (8) Nolan, M.; Elliott, S. D. *Phys. Chem. Chem. Phys.* **2006**, *8*, 5350.
- (9) Mahalingam, T.; Chitra, J. S. P.; Chu, J. P.; Moon, H.; Kwon, H. J.; Kim, Y. D. *J. Mater. Sci.: Mater. Electron.* **2006**, *17*, 519.
- (10) Kunze, J.; Maurice, V.; Klein, L. H.; Strehblow, H.-H.; Marcus, P. *J. Phys. Chem. B* **2001**, *105*, 4263.
- (11) Ambrose, J.; Barradas, R. G.; Shoesmith, D. *J. Electroanal. Chem.* **1973**, *47*, 47.
- (12) Droog, J. M. M.; Alderliesten, C. A.; Alderliesten, P. T.; Bootsma, G. A. *J. Electroanal. Chem.* **1980**, *111*, 61.
- (13) Martins, M. E.; Arvia, A. J. *J. Electroanal. Chem.* **1984**, *165*, 135.
- (14) Gennero de Chialvo, M. R.; Zerbino, J. O.; Marchiano, S. L.; Arvia, A. J. *J. Appl. Electrochem.* **1986**, *16*, 517.
- (15) Burke, L. D.; Ryan, T. G. *J. Electrochem. Soc.* **1990**, *137*, 1358.
- (16) Hodes, Gary., *Chemical Solution of Deposition Semiconductor Films*; Marcel Dekker: New York, 2002.
- (17) Härtinger, S.; Pettinger, B.; Doblhofer, K. *J. Electroanal. Chem.* **1995**, *397*, 335.
- (18) Chan, H. Y. H.; Takoudis, C. G.; Weaver, M. J. *J. Phys. Chem B* **1999**, *103*, 357.
- (19) Matsuoka, O.; Ono, S. S.; Nozoye, H.; Yamamoto, S. *Surf. Sci.* **2003**, *545*, 8.
- (20) Maurice, V.; Strehblow, H.-H.; Marcus, P. *Surf. Sci.* **2000**, *458*, 185.
- (21) Strehblow, H.-H.; Maurice, V.; Marcus, P. *Electrochim. Acta* **2001**, *46*, 3775.
- (22) Kang, M.; Gewirth, A. A. *J. Phys. Chem B* **2002**, *106*, 12211.
- (23) Kautek, W.; Geuß, M.; Sahre, M.; Zhao, P.; Mirwald, S. *Surf. Interface Anal.* **1997**, *25*, 548.
- (24) Kunze, J.; Maurice, V.; Klein, L. H.; Strehblow, H.-H.; Marcus, P. *J. Electroanal. Chem.* **2003**, *554–555*, 113.
- (25) He, J.-B.; Lu, D.-Y.; Jin, G.-P. *Appl. Surf. Sci.* **2006**, *253*, 689.
- (26) Jovic, V. D.; Jovic, B. M. *J. Serb. Chem. Soc.* **2002**, *67*, 531.
- (27) Chu, Y. S.; Robinson, I. K.; Gewirth, A. A. *J. Chem. Phys.* **1999**, *110*, 12–5952.
- (28) Nakaoka, K.; Ueyama, J.; Ogura, K. *J. Electrochem. Soc.* **2004**, *151*, C661.
- (29) Maurice, V.; Strehblow, H. H.; Marcus, P. *J. Electrochem. Soc.* **1999**, *146*, 524.
- (30) Raebiger, H.; Lany, S.; Zunger, A. *Phys. Rev. B* **2007**, *76*, 045209.
- (31) Fernandez, A. M.; Turner, J. A. *Sol. Energy Mater. Sol. Cells* **2003**, *79*, 391.
- (32) Rakshani, A. E. *J. Appl. Phys.* **1991**, *69*, 2365.
- (33) Wright, A. F.; Nelson, J. S. *J. Appl. Phys.* **2002**, *92*, 5849.
- (34) Rakshani, A. E.; Makdisi, Y.; Mathew, X. *Thin Solid Films* **1996**, *288*, 69.
- (35) Yang, W. Y.; Rhee, S. W. *Appl. Phys. Lett.* **2007**, *91*, 232907.
- (36) Rosenstock, Z.; Feldman, I.; Gil, Y.; Riess, I. *J. Electroceram.* **2005**, *14*, 205.
- (37) Díez-Pérez, I.; Sanz, F.; Gorostiza, P. *Curr. Opin. Sol. Stat. Mater. Sci.* **2006**, *10*, 144.
- (38) Díez-Pérez, I.; Gorostiza, P.; Sanz, F. *J. Electrochem. Soc.* **2003**, *150*, B348.

- (39) Güell, A. G.; Díez-Pérez, I.; Gorostiza, P.; Sanz, F. *Anal. Chem.* **2004**, *76*, 5218.
- (40) Díez-Pérez, I.; Güell, A. G.; Sanz, F.; Gorostiza, P. *Anal. Chem.* **2006**, *78*, 7325.
- (41) Díez-Pérez, I.; Sanz, F.; Gorostiza, P. *Electrochem. Commun.* **2006**, *8*, 1595.
- (42) Díez-Pérez, I.; Vericat, C.; Gorostiza, P.; Sanz, F. *Electrochem. Commun.* **2006**, *8*, 627.
- (43) Díez-Pérez, I.; Gorostiza, P.; Sanz, F.; Müller, C. *J. Electrochem. Soc.* **2001**, *148*, B3207.
- (44) *Powder Diffraction File Database*; International Center for Diffraction Data: Newtown Square, PA, 1997.
- (45) Horcas, I.; Fernandez, R.; Gomez-Rodriguez, J. M.; Colchero, J.; Gomez-Herrero, J.; Baro, A. M. *Rev. Sci. Instrum.* **2007**, *78*, 013705.
- (46) Gerischer, H. *Corros. Sci.* **1989**, *29*, 191.
- (47) Gomes, W. P.; Vanmaekelbergh, D. *Electrochim. Acta* **1996**, *41*, 967.
- (48) Tsuchiya, H.; Macak, J. M.; Ghicov, A.; Arlindo; Räder, S.; Taveira, L.; Schmuki, P. *Corros. Sci.* **2007**, *49*, 203.
- (49) Madelung, O.; Rössler, U.; Schulz, M. *Non-Tetrahedrally Bonded Elements and Binary Compounds I, Landolt-Börnstein-Group III Condensed Matter, Numerical Data and Functional Relationships in Science and Technology*; Springer-Verlag: Heidelberg, Germany, 1998.
- (50) Deleted in proof.
- (51) Mizuno, K.; Izaki, M.; Murase, K.; Shinikawa, T.; Chigane, M.; Inaba, M.; Tasaka, A.; Awakura, Y. *J. Electrochem. Soc.* **2005**, *152*, C-179.

JP805915A